Fast and accurate rat head motion tracking with point sources for awake brain PET

Fast and accurate rat head motion tracking with point sources for awake brain PET

Alan Miranda, Steven Staelens, Sigrid Stroobants and Jeroen Verhaeghe

***Abstract*— To avoid the confounding effects of anesthesia and immobilization stress in rat brain positron emission tomography (PET), motion tracking based unrestrained awake rat brain imaging is being developed. In this work we propose a fast and accurate rat head motion tracking method based on small PET point sources. PET point sources (3-4) attached to the rat's head are tracked in image space using 15-32 ms time frames. Our point source tracking (PST) method was validated using a manually moved microDerenzo phantom that was simultaneously tracked with an optical tracker (OT) for comparison. The PST method was further validated in three awake [^{18}F]FDG rat brain scans. Compared to the OT, the PST based correction at the same frame rate (31.2 Hz) reduced the reconstructed FWHM by 0.39 – 0.66 mm for the different tested rod sizes of the microDerenzo phantom. The FWHM could be further reduced by another 0.07 – 0.13 mm when increasing the PST frame rate (66.7 Hz). Regional brain [^{18}F]FDG uptake in the motion corrected scan was strongly correlated ($p<0.0001$) with that of the anesthetized reference scan for all three cases ($0.94 < r < 0.97$). The proposed PST method allowed excellent and reproducible motion correction in awake *in vivo* experiments. In addition, there is no need of specialized tracking equipment or additional calibrations to be performed, the point sources are practically imperceptible to the rat and PST is ideally suitable for small bore scanners where optical tracking might be challenging.**

***Index Terms*—Nuclear imaging, animal models and imaging, motion compensation**

I. Introduction

POSITRON emission tomography (PET) is used to investigate *in vivo* functional processes of biomolecules. In small animal PET neurological research both the use of anesthesia and the effects of stress induced by restraining can be confounding factors in the brain response [1-6]. To avoid the unwanted and often poorly understood effects of anesthesia and stress on the PET response, methods to perform scans of awake and unrestrained animals have been proposed [7-10].

Some of the current methods to perform brain scans of awake and unrestrained rats rely on tracking the rigid body motion of the rat head during the PET scan. Using the motion information, the measured lines of response (LORs) are repositioned to a reference position during reconstruction [11]. This technique allows PET reconstructions of the brain as if the subject had not moved. In previous work the tracking has been performed using optical cameras (optical tracking, OT), e.g. by measuring the pose (6 degrees of freedom) of specially designed markers attached to the rat head [12], or by markerless motion tracking that detects distinct features on the rat head [13]. These methods require a spatial calibration between the optical tracking device and the PET scanner coordinate system as well as a time synchronization to relate the camera measured motion to the PET LORs. These two procedures have an associated error which affects the quality of the motion corrected reconstructions [14]. Furthermore, optical tracking can be challenging in small bore scanners due to the occluded view of the rat's head. In addition, when using tracking devices that use optical markers to measure the motion, it can be difficult to prevent small independent motion of the markers due to slippage (skin motion).

In this work we develop a method that uses ultra small PET point source grains to track the head motion during the PET scan (point source tracking, PST). The pose of the rat head is determined by measuring the position of at least 3 non-collinear radioactive point source grains attached to the rat's head. This method thus makes use of detection by the PET scanner itself to track the motion and therefore neither spatial calibration nor time synchronization is needed, avoiding associated errors with these procedures. Furthermore, we have made the point sources small and light enough to be almost imperceptible for the rat reducing unsettling sensations as well as being less prone to slippage.

II. Methods

A. Experimental setup

In this work we used a Siemens Inveon microPET scanner (Siemens Medical Solutions, Inc., Knoxville, USA). The scanner consists of 4 rings of 16 blocks, each with 20 × 20 crystals of lutetium orthosilicate (LSO) with crystal size of 1.5 × 1.5 × 10 mm. The scanner's axial length is 127 mm with a diameter of 161 mm [15]. The bore diameter is 120 mm while the transaxial field of view (FOV) is 100 mm. The scanner default energy window (350 to 650 keV) was used for all experiments. The scanner sensitivity at the center of the FOV (CFOV) is 6.8 %. Images are reconstructed into a 128×128×159 grid with voxel size of 0.776×0.776×0.796 mm along the x, y and z axis respectively.

Alan Miranda, Jeroen Verhaeghe and Steven Staelens are with the Molecular Imaging Center Antwerp, University of Antwerp, Antwerp, Belgium.

Sigrid Stroobants is with the Antwerp University Hospital, Antwerp, Belgium.

The point sources used to perform the motion tracking are made of sodium polyacrylate $[CH_2CH(CO_2Na)]_n$ grains. The grains were carefully selected so that their size was smaller than 1 mm in diameter. The grains were then soaked for 10 s in hematoxylin colorant used for better visualization when pasting the grain on the white fur of the rat (coloring is not important for motion tracking). Finally the grains were soaked for 5 s in [^{18}F]FDG. Immediately after FDG absorption the activity of the grain was measured. If the activity was lower than 148 kBq (4 μCi) the grain was soaked for another 5 s in FDG to increase its activity. Finally only grains with an activity within the range of 148-222 kBq (4-6 μCi) were used as point sources for tracking. The weight of each point source was about 300 μg.

To compare the performance of the PST with that of OT (phantom experiment only), a Micron Tracker Sx60 (Claron Technology Inc., Toronto, Canada) stereo vision camera was used as previously described [14]. This OT device was spatially calibrated with the PET scanner by simultaneously measuring the positions of a 35×30 mm checkerboard marker and a radioactive point source pasted on its surface. Twenty different positions were measured and the cross-calibration matrix between the OT and PET scanner measurements was found through least squares minimization. The calibration is then used to transform the measured motion to PET coordinates. The time synchronization between the OT and the PET scanner was performed using an Arduino Uno (Arduino SA) microcontroller, which sends a square wave signal to trigger the OT, which in turn sends a strobe signal to the gating input of the PET scanner. A few seconds before the end of the PET scan the frequency of the square wave signal changes to an irregular pattern which is used to temporally align the OT motion information with the list-mode data gate tags.

B. Tracking algorithm

The tracking algorithm works by identifying the position of point sources in the image space. At least 3 non-collinear point sources in a rigid configuration are used to uniquely determine the pose of the object they are attached to. The minimum tracking frame rate used was 31.2 Hz (32 ms frame duration). The short time frame images in which the point sources are identified are approximate reconstructions (to reduce calculation time) of the LORs. The generation of these images and the tracking algorithm using these images are explained below.

1) Approximate reconstruction. The reconstructed images are denoted as f_j the image intensity at voxel j, where j is the linear index of voxel with coordinates (x, y, z) $(j = 1, \dots, J)$. The image was reconstructed by performing 3 iterations of the list-mode expectation maximization algorithm [16]:

$$f_j^{q+1} = \frac{f_j^q}{\sum_{r=1}^{R} w_r a_{rj}} \sum_{i=1}^{I} a_{ij} \frac{1}{\sum_{b=1}^{J} a_{ib} f_b^q} \quad (1)$$

where f_j^q is the intensity of voxel j at iteration q, a_{ij} is the probability of a photon pair emitted at voxel j being detected along LOR i, w_i is the normalization factor for LOR i and R is the total number of possible LORs. Probability a_{ij} was calculated on-the-fly using Siddon's algorithm [17]. The image f_j was finally filtered 3 times with a 3×3×3 mean filter. The image calculated in this way will be referred to as IEM (image expectation maximization).

2) Point source tracking algorithm. To initialize the tracking algorithm the identification index of the point sources to be tracked p $(p = 1, \dots, P)$ and their inter-point distances m_l $(l = 1, \dots, L)$, with $L = C_2^P$ the number of 2 combinations from a set with P elements, are used as a model to identify the correct point sources. To measure the inter-point distances of the model, the approximate reconstruction IEM is used. The approximate reconstruction of the first time frame is visually inspected. Once the point sources are manually located their index and spatial coordinates are recorded as model.

The list mode data LORs are first ordered into consecutive time frame blocks with equal duration. The blocks are divided using the time tags which are present every 0.2 ms in the list mode data. Then the approximate reconstruction IEM using the time frame LORs is calculated. Next, a grayscale dilation [18] is applied to the approximate reconstructions:

$$(f \oplus \kappa)(x, y, z) =$$

$$\max\{f(x - x', y - y', z - z') | (x', y', z') \in D_\kappa \setminus (0,0,0)\} \quad (2)$$

where κ is a 5×5×5 kernel, D_κ is the domain of the 5×5×5 kernel κ and f is assumed to be $-\infty$ outside the image domain. This operation replaces every voxel by the maximum in the 5×5×5 voxels vicinity without considering the voxel itself. Then, the original image f is compared with the dilated image and the coordinate of the voxels where $f > (f \oplus \kappa)$ are selected as local maxima points. Due to the high noise in the approximate reconstructions several low intensity maxima were present. By applying a lower threshold to the maxima most local maxima that do not correspond to the point sources were removed. The threshold was empirically selected based on the fact that the intensity of the point sources is above that of most of the local maxima.

Once these local maxima have been determined, the point source locations are found amongst them. If the point sources were found in the previous frame then the distance from these locations to all current local maxima is calculated and the closest local maximum within a small tolerance (3 mm in our experiments) is selected. If such a nearby point is found for all the previous point source positions, these nearby points are selected as the point sources locations in the current frame; otherwise, and also in the case the point sources were not found in the previous frame, the following algorithm is used to find the point source locations.

A 7×7×7 neighborhood is taken around each of the local maxima $(n = 1, \dots, N)$ and a binary image is formed by applying a threshold at 65 % of the maximum in the neighborhood. From this binary image the volume v_n (i.e. the number of voxels equal to 1) and the compactness $c_n \in (0,1]$

[19] are calculated for each local maximum n. The compactness is a measure that quantifies the similarity of a binary shape B with a sphere and is calculated as:

$$c(B) = \frac{3^{5/3}}{5(4\pi)^{2/3}} \cdot \frac{\mu_{0,0,0}(B)^{5/3}}{\mu_{2,0,0}(B)+\mu_{0,2,0}(B)+\mu_{0,0,2}(B)} \quad (3)$$

where $\mu(B)$ are the central moments [18, 19] of the binary shape B and the subindex indicate the order of the moment in x, y, z respectively.

Finally the following score is calculated:

$$S_n = e^{-v_n/V} e^{(c_n-1)/C} \quad (4)$$

where S_n is the score of local maximum n, and V and C are constants defined empirically to be 80 voxels and 0.3 respectively. The score is closer to 1 when the binary shape is small or/and its shape is similar to a sphere (i.e. its compactness is closer to 1). Then 10 points corresponding to the 10 highest scoring local maxima are selected and the inter-point distances matrix (10×10 symmetric square matrix) between these points is calculated.

This matrix is used to form g groups containing P points. The total number of groups that can be formed is P-permutations of 10. The groups for which at least one inter-point distance is not within a predefined threshold (1.7 mm in our experiments) from the models distances m_l are then discarded. If there are no groups with inter-point distances within the predefined threshold the tracking fails for the current frame, otherwise the group error E_g between group g and the model group is calculates as

$$E_g = \sum_{l=1}^{L} \left| D_l^g - m_l \right| \quad (5)$$

where D_l^g is the l-th inter-point distance of group g. The group that most closely resembles the model, i.e. the group that minimizes E_g, is then selected as the point source locations in the current frame.

To reduce the computational load of finding the point source locations, the image volume in which the point sources are searched for can be reduced to a smaller neighborhood around the previous point sources locations if these were identified correctly. This neighborhood was set to a box that extends the box enclosing all point sources previous locations by 8 mm. This was done here after the approximate reconstruction.

The resolution of the point source locations ($\boldsymbol{c}_v$) is initially limited by the voxel resolution. To further refine the resolution to a sub-voxel accuracy all the LORs that pass within 3 mm from the initial center $\boldsymbol{c}_v$ are considered. From these LORs the final point source location $\boldsymbol{c}_p$ corresponding to the point that minimizes the average distance to all these LORs [20] is calculated as

$$\boldsymbol{c}_p = argmin_{\boldsymbol{c}} \Sigma_i \boldsymbol{D}^{(i)}(\boldsymbol{c}) \quad (6)$$

where, $\boldsymbol{D}^{(i)}$ is the vector from point $\boldsymbol{c}$ to LOR i.

Finally, after the point sources have been located throughout the whole scan, the pose in each time frame is determined by point set registration, which involves the calculation of the singular value decomposition of the cross-covariance matrix between the measured point sources and the model point sources coordinates [21]. As the point sources are described in PET coordinates the corresponding motion is calculated directly in PET coordinates as well. The pseudocode for the point source tracking algorithm can be found in appendix 1. The tracking algorithm was implemented in Matlab (The Mathworks, Inc. Natick, United States). For the approximate reconstruction a parallelized C library was called.

3) Skin slippage correction. The point source model that defines the inter-point distances m_l and that is used for the point set registration was obtained from the initial frame. This method was suitable for the phantom experiments. However, in the rat experiments, due to the flexibility of the rat skin, the frame inter-point distances could change over the course of the scan. As a consequence, when determining the error between the model and the local maxima inter-point distances, correct point sources position could be rejected if, due to the skin motion, the true inter-point distances differed from the original model inter-point distances threshold. To avoid this the model inter-point distances were constantly recalculated for each frame as the mean of the inter-point distances in the 5 previous correctly tracked frames. To avoid introducing too large errors in the pose estimation, after all frames have been tracked, a single fixed point set model was considered for the point set registration. Frames for which the point set registration error was more than 1 mm were then discarded from the reconstruction.

The fixed point set model is calculated as follows. First the point source positions are determined for all frames, and are spatially aligned to the point source positions in the first frame, corresponding to the initial point set model. Then the average position (centroid) of the aligned point sources is calculated. These centroid positions define the final point set model.

C. Validation experiments

1) Tracking accuracy. To validate the tracking accuracy of PST and OT a microDerenzo phantom (3, 2.5, 2, 1.5 and 1.25 mm diameter rods, double diameter spacing) was moved using the scanner bed motion control system (Velmex, Inc., Bloomfield, United States). The phantom was simultaneously tracked with PST and OT at 31.2 Hz. The accuracy of the bed motion is 0.08 mm. The initial activity of the phantom was 25 MBq of [^{18}F]FDG. A checkerboard marker of 28×23 mm was attached to the front of the phantom and three PET point sources were pasted onto the surface of the phantom for OT and PST respectively. The distances between the point-sources were 26.4, 42.7 and 49.3 mm.

First, the transformation between PST and OT reference

position measured in PET coordinates to the scanner bed position was calculated by measuring 5 static positions along the axial axis (z axis) at 4 vertical positions (y axis), i.e. 20 positions in total, simultaneously with PST and OT. The transformation to bed positions was then found through least-square minimization of the distance between paired measurements for both PST and OT.

Next, the phantom was placed at 4 different positions (10, 20, 30 and 40 mm) along the y axis and moved along the axial axis 85 mm from one axial extreme of the FOV to the other at a constant speed (2 cm/s). At y = 10 mm the bottom of the phantom was completely at the lower vertical extreme of the scanner FOV and at 40 mm the top of the phantom was at the upper vertical extreme. Positions were measured during motion using both OT and PST. These positions were then transformed to bed positions using the previously calculated transformation matrix. The mean translational position error along the axial axis at each of the 4 vertical positions was calculated as

$$E^{PST} = \frac{1}{H}\sum_{h=1}^{H}\left\|P_h^{PST} - P_h^{bed}\right\| \qquad (7)$$

where P_h^{PST} is the estimated position by PST, P_h^{bed} is the true bed position defined by the bed control system and H is the number of positions measured during motion. Correspondingly the mean error E^{OT} for OT was calculated.

2) Image reconstruction. Phantom and *in vivo* PET experiment were reconstructed using in house reconstruction software. Motion-free reconstructions were performed using an ordered subsets implementation of (1) [26] with 16 subsets and 8 iterations. LOR efficiency normalization factors were considered for the calculation of the sensitivity image. Attenuation, scatter and randoms correction was not considered. Image space based resolution modeling was included in the reconstruction algorithm [27] using a 1.2 mm full width at half maximum (FWHM) Gaussian kernel. The reconstruction algorithm that was used for the motion free case was extended to enable motion correction [28]. Again the reconstruction did not include attenuation, scatter and randoms correction but did include resolution modeling (1.2 mm FWHM). The motion dependent sensitivity image was calculated through cubic interpolation in the image space using the approach described in [28].

3) Image resolution. The microDerenzo phantom described above was manually moved during a 10 minutes PET scan. The initial activity of the phantom was 22 MBq of [^{18}F]FDG and the PET scan duration was 10 minutes. In addition a 10 minutes motion-free scan of the phantom was performed for comparison. During scanning the phantom was simultaneously tracked with PST and OT methods at 31.2 Hz. A checkerboard marker of 28×23 mm was used for OT. The distance between PST point-sources was 50.3, 26.8 and 43.8 mm.

In addition, the OT motion was filtered with a finite impulse response filter using a Gaussian window with FWHM of 100 ms [22-23]. In addition to the tracking at 31.2 Hz, PST was also performed using 20 ms (50 Hz) and 15 ms (66.7 Hz) time frames to observe the effect of the tracking frame rate on the tracking accuracy and the spatial resolution of the motion corrected reconstructions using PST.

The FWHM of the phantom rods in the motion-free and the motion corrected images using respectively the OT and PST motion information was measured in an average of 8 slices in the transverse plane. For profiles where more than one rod was present, a sum of Gaussians function, with the number of Gaussians equal to the number of rods, was fitted to the profile and the average FWHM and standard deviation was calculated for the 3, 2.5, 2 and 1.5 mm rod groups.

Finally, the uncertainty in the motion measurement for both tracking systems was determined by calculating the standard deviation from the mean position using 200 motion samples from the motion free acquisition.

4) Awake rat brain experiments. Three awake Sprague-Dawley rats were scanned and tracked using the PST. The animals were treated in accordance with the European Ethics Committee (decree 86/609/CEE) and the animal experiment was approved by the Animal Experimental Ethical Committee of the University of Antwerp, Antwerp, Belgium (ECD 2011-54). Four point sources were used for the tracking. To attach the point sources to their head the rats were anesthetized (isoflurane in medical oxygen 5% for induction, 2 % for maintenance). Patches of fur were shaved to allow pasting the point sources (Fig. 1 (a)). The point sources were pasted on the skin using cyanoacrylate glue. One point source was pasted bellow each ear and two were pasted on the nasal bridge. The maximal and minimal distance between point sources was 35 and 9 mm respectively. Afterwards the rats were administered 37 MBq of [^{18}F]FDG through tail vein injection. Immediately after injection, anesthesia was stopped and the rats were left 20 minutes awake for [^{18}F]FDG uptake. Then the rats were placed inside a plastic container (10 cm inner diameter, 17 cm length) with transparent lids containing ventilation holes (Fig. 1 (b)). The container was then placed on the scanner bed approximately aligning the rat head with the scanner CFOV. After positioning, a 20 minute scan of the awake rats was performed. The rats could move freely (Fig. 1(b)) in the container during the whole scan (grooming, move back and forth, etc.). At the end of the scan the rats were anesthetized again (5% for induction, 2% for maintenance) and positioned on the scanner for a 20 minutes (except for rat 2: 10 minutes due to technical issue) motion-free scan for comparison. In all cases the tracking frame rate was 31.2 Hz.

The brain uptake (normalized to cerebellum) for 34 predefined brain regions, including several cortical subregions (visual, auditory and cingulate), hypothalamus and cerebellum (W. Schiffer brain atlas [24]), was measured using PMOD 3.7 (PMOD technologies Ltd, Zurich, Switzerland). All reconstructions were aligned through a rigid body transformation. Afterwards, the rat [^{18}F]FDG brain uptake atlas and its brain regions were aligned and spatially normalized to the anesthesia scan. The mean voxel value in each region of the brain atlas was calculated and normalized to

the cerebellum mean value. The relative [^{18}F]FDG uptake from the anesthesia reference scan and the corrected and uncorrected awake scan were compared using a Bland-Altman plot [25], as well as by calculating the Pearson's r correlation coefficient.

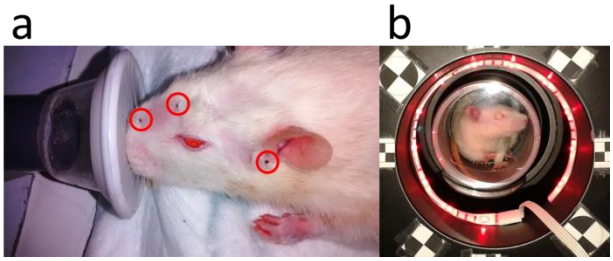

Fig. 1. (a) Rat under anesthesia showing 3 of the 4 point sources used for motion tracking. (b) Awake rat inside the cylindrical holder during the PET scan. Red LED lights were used for better visualizing of the rat inside the scanner bore. Checkerboard markers only used for the phantom experiment using OT.

5) Spatial resolution scaling. As a measure to assess the spatial resolution difference between the motion corrected and the motion-free reconstructions a spatially invariant Gaussian filtering at different scales (σ^2= 0 - 2.88 mm^2) was applied to the motion-free reconstructions. The image correlation between the motion corrected images and the filtered motion-free reconstructions (each with a different σ^2) was calculated. The scale parameter, i.e. σ^2 of the Gaussian kernel [29], of the filtered motion-free reconstructions which maximizes the image correlation with the motion corrected images was selected as the scale parameter of the motion corrected images. The magnitude of the scale parameter is proportional to the difference between images. The scale parameter not only reflects loss of spatial resolution but also depends on the noise level and, in the case of the rat experiments, on the differences in [^{18}F]FDG uptake between the awake and anesthesia scans.

III. Results

A. Tracking algorithm

The average tracking computation time of a frame with 9000 LORs was 196 ms for the IEM reconstruction. From all steps of the algorithm, the image dilation used to determine the image local maxima was the most time consuming calculation. However, when the search volume could be reduced to a neighborhood around the point source locations of the previous frame, the image dilation calculation time on the smaller volume reduces significantly (one order of magnitude).

The tracking success rate is shown in Table 1. In all cases the tracking success rate is higher than 90%. For the microDerenzo phantom most of the tracking fail is due to the phantom moved out of the FOV. Both at 31.2 and 50 Hz the tracking success rate is 95 %. However at 66.7 Hz the tracking success rate is reduced to 91.3 %. For the rat experiments rat 3 has the lowest tracking success rate. In about 1.5 min of the 20 min scan rat 3 was not tracked.

The PET data pertaining to frames where tracking failed were discarded from the motion corrected reconstruction.

TABLE I
TRACKING SUCCESS RATE USING THE IEM APPROXIMATE RECONSTRUCTION FOR THE MICRODERENZO (MD) AND RAT EXPERIMENTS

Experiment					
mD 31.2 Hz	mD 50 Hz	mD 66.7 Hz	Rat 1	Rat 2	Rat3
Tracking success rate					
95.1 %	95.2 %	91.3 %	97.2 %	98.7 %	92.5 %

For the skin slippage correction, the range of the standard deviation of the inter-point distances measured over the 3 awake rat scans was 0.59-0.95 mm due to the skin flexibility, in comparison with 0.31-0.43 mm for phantom experiments where no inter-point distance change is expected. Only about 50 frames in 36000 frames were discarded due to extreme change in the inter-point distances.

B. Accuracy

1) OT cross-calibration accuracy. The mean and maximum error over the 20 calibration point source positions measured by OT and PET scanner was 0.36 and 0.58 mm respectively.

2) Tracking accuracy. Fig. 2 (a) shows the mean tracking error E^{PST} and E^{OT} for motion along the z axis for 4 vertical positions of the phantom. In all cases E^{OT} is smaller than E^{PST} and the error is similar for all y axis positions. The mean error for PST and OT over all positions is 0.24 ± 0.07 and 0.19 ± 0.05 mm respectively. Both PST and OT show good agreement with the motion defined in the scanner bed system as can be seen in Fig. 2 (b).

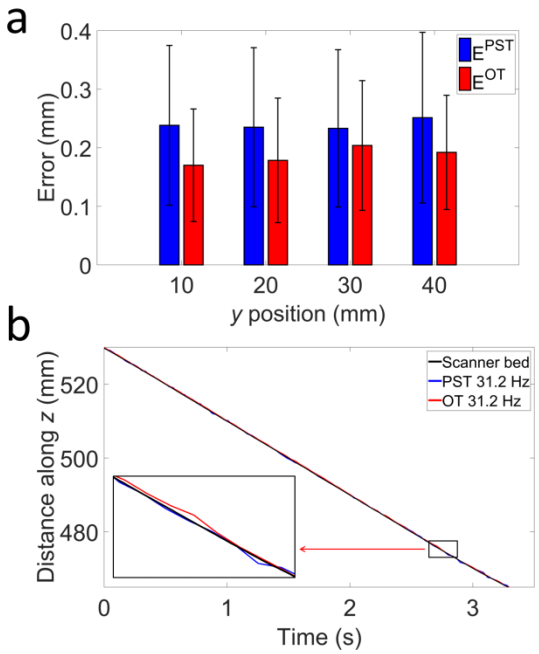

Fig. 2. a) Translational motion tracking error for PST and OT for motion along the z axis at 4 different positions along the vertical y axis. b) Sample of the motion y = 40 mm as measured by the different systems.

C. Image resolution

The average speed of the phantom measured at the centroid

of the point sources (close to the center of the phantom) was 4.03 cm/s. In Fig. 3 (a) the translation of the phantom along the x axis and (b) the rotation about the y axis measured with the OT (31.2 Hz) and the PST (31.2 Hz) is shown. The OT unfiltered motion shows higher noise in comparison with the point source tracking motion. No temporal delay is observed between the OT and PST. When measuring a static position the standard deviation in the measurement is 131 μm for the OT and 73.5, 96 and 103 μm for PST at 31.2, 50 and 66.7 Hz respectively.

Fig. 4 shows the transverse slice of the reconstructions for the (a) motion-free, (b) motion corrected using OT (31.2 Hz) and motion corrected using PST with (c) 31.2 and (d) 66.7 Hz. In Fig. 5, profiles trough the 3, 2.5 and 2 mm rods show a greater degradation of spatial resolution in the motion corrected reconstruction using the OT in comparison to the PST at the same frame rate. Table 2 shows the FWHM in the motion-free, OT, OT filtered (31.2 Hz) and PST (31.2, 50 and 66.7 Hz) motion corrected reconstructions for the different rods. In all cases the OT based method results in the largest FWHM values with a slight decrease after filtering the OT data. When increasing the PST tracking rate, slightly improved spatial resolution in the motion corrected reconstructions is observed, as seen in Fig. 5 and Table 2.

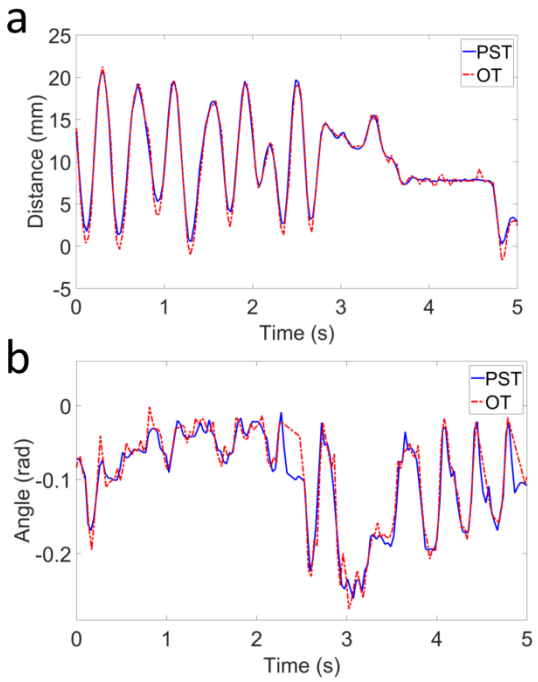

Fig. 3. (a) Translation along the x axis and (b) rotation about the y axis measured using PST and OT respectively.

TABLE II
FWHM ± STD (MM) FOR THE 1.5, 2, 2.5 AND 3 MM RODS IN THE MOTION-FREE AND MOTION CORRECTED RECONSTRUCTIONS USING PST, OT AND FILTERED (F) OT DATA

Reconstruction	Rods diameter (mm)			
	1.5	2	2.5	3
Motion-free	2.14±0.12	2.21±0.07	2.24±0.07	2.65±0.04
OT w/o F 31.2 Hz	3.20±0.55	2.97±0.14	3.08±0.11	3.44±0.10
OT w F 31.2 Hz	3.17±0.57	2.94±0.15	3.07±0.10	3.36±0.07
PST 31.2 Hz	2.54±0.20	2.55±0.07	2.69±0.04	2.93±0.03
PST 50 Hz	2.44±0.13	2.46±0.05	2.60±0.03	2.87±0.03
PST 66.7 Hz	2.41±0.14	2.44±0.05	2.56±0.03	2.86±0.05

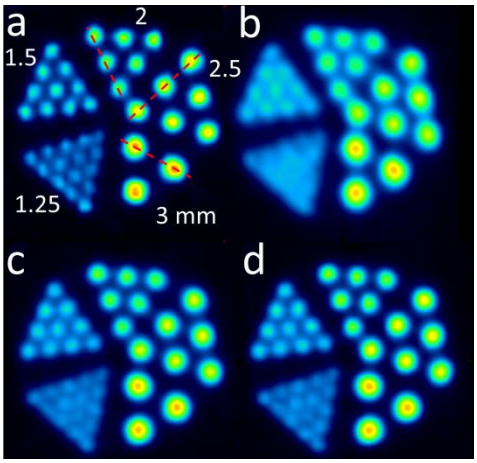

Fig. 4. Transverse slice (one voxel thickness, 0.796 mm) of the microDerenzo phantom reconstructions for the (a) motion-free scan, (b) motion corrected scan with OT and motion corrected scans with PST at (c) 31.2 and (d) 66.7 Hz. Profiles of red lines on (a) are shown in Fig. 5.

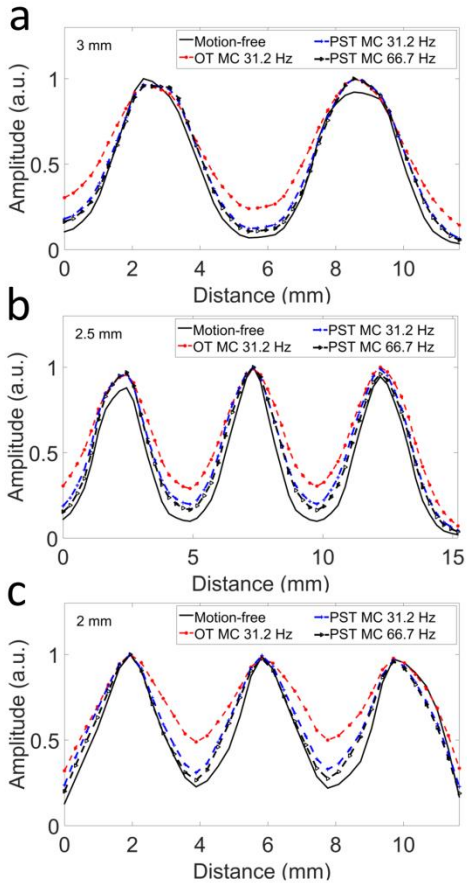

Fig. 5. Profile through the motion-free and motion corrected reconstructions of the microDerenzo phantom rods (red dotted lines on Fig. 4 (a)) with OT at 32.1 Hz and PST at 32.1 and 66.7 Hz for the (a) 3, (b) 2.5 and (c) 2 mm rods.

Table 3 shows the scale parameter for all motion corrected reconstructions of the microDerenzo phantom. In all cases the scale parameter is smaller using PST and decreases with increasing tracking frame rate. For the OT, filtering of the poses reduces the scale parameter.

TABLE III
SCALE PARAMETER FOR THE MOTION CORRECTED RECONSTRUCTIONS USING PST, OT AND FILTERED (F) OT DATA

Reconstruction	Scale parameter (mm^2)
OT w/o F 31.2 Hz	0.52
OT w F 31.2 Hz	0.46
PST 31.2 Hz	0.22
PST 50 Hz	0.20
PST 66.7 Hz	0.18

D. Awake rat experiments

The average translational speed of the rat's head measured at the centroid of the point sources (close to the brain medial prefrontal cortex) was 0.510, 0.407 and 0.538 cm/s for the rat 1, 2 and 3 respectively. In all cases the reconstructions are greatly degraded due to the motion of the rat, as shown in Fig. 7. After motion correction the structure of the rat brain is recovered and regions such as the cortex, hippocampus and cerebellum can be identified. The motion corrected reconstructions show good agreement with the reconstructions using anesthesia.

Table 4 shows that there is a strong correlation between the motion corrected awake and anesthesia reconstructions whereas correlation is much poorer for the uncorrected awake scan.

Fig. 6 shows that the 95% limits of agreement for the awake images uptake is 71%, reduced to 22.7% after motion correction of the awake images.

TABLE IV
PEARSON'S r CORRELATION COEFFICIENT FOR THE ANESTHESIA VERSUS AWAKE SCAN RECONSTRUCTIONS AND FOR THE ANESTHESIA VERSUS AWAKE SCAN MOTION CORRECTED RECONSTRUCTIONS. SIGNIFICANCE LEVEL $p^{*} < 0.05$, $p^{****} < 0.0001$.

	Rat 1	Rat 2	Rat 3
Awake	0.424 *	0.528	0.385 *
Awake MC	0.974 ****	0.939 ****	0.943 ****

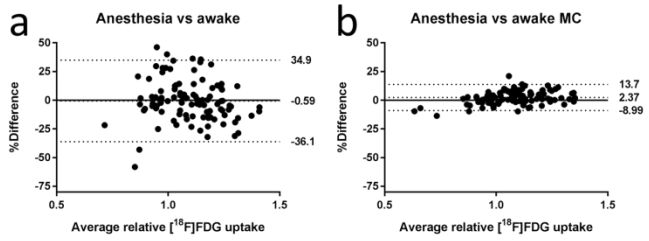

Fig. 6. Bland-Altman plot for the anesthesia scan versus (a) awake and (b) awake motion corrected images brain regional [^{18}F]FDG relative uptake. The upper, middle and lower dotted lines mark the 95% upper limit of agreement, bias and 95% lower limit of agreement respectively.

The scale parameter of the motion corrected image for rat 1, 2 and 3 was respectively 0.58, 0.30 and 0.41 mm^2. Difference between motion corrected and anesthetized reconstructions in all 3 cases are small (less than 1 mm σ) compared to the scanner spatial resolution (1.5 mm) [15].

IV. DISCUSSION

Radioactive point sources were used to track rigid head motion during PET scans. The frame rate at which the point sources could be tracked *in vivo* is sufficiently high to perform motion correction in awake rat brain scans. The image based tracking algorithm used for the point source identification was robust enough to detect the point sources in 32, 20 and 15 ms time frames. Several factors impact the feasibility of the motion tracking as well as its accuracy. Some of these factors are: the scanner spatial resolution and sensitivity, the activity of the point sources, the quality of the short time frame reconstructions, the tracking frame rate, the distance of the point sources to the subject's activity, the inter-point distances and the number of point sources used for the motion tracking.

The scanner spatial resolution determines the uncertainty in the localization of a point source. In an initial step the point source positions are determined in the image space in the voxel grid. Therefore its localization uncertainty depends on the voxel size. In a second step, the point source coordinates are further refined using the individual LORs of the point source. Therefore, the final position uncertainty is not limited by the reconstruction voxel size. Moreover, when using several point sources to determine a single position, the uncertainty reduces by calculating the average position (centroid) of the point sources rigid configuration. For the used scanner with crystal pixel size of 1.5 mm, the standard deviation in position determination using 3 point sources was 73.5 μm. Furthermore, temporal filtering can be applied to the individual point source positions to reduce the uncertainty, but the filter parameters must be defined so that the motion is not oversmoothed. In preliminary tests (data not shown) such an additional filtering of the locations did not improve the image quality of the motion corrected reconstructions. Therefore we did not consider temporal filtering PST in our current experiments for clarity.

The activity of the point sources, the sensitivity of the PET scanner and the quality of the short time frame reconstructions determine the minimum duration of the frames in which the point sources can be localized. The point sources must have enough activity to be distinguished in the short time reconstructions used in the tracking algorithm.

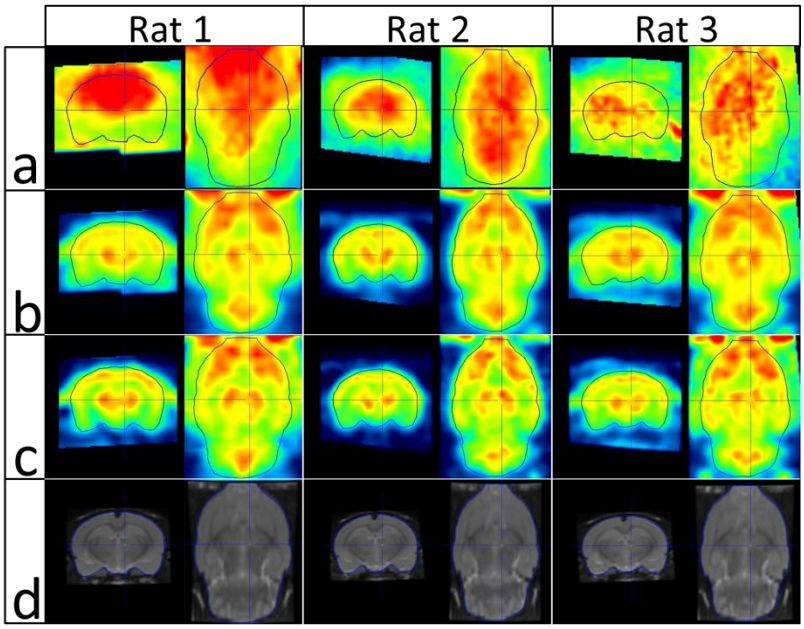

Fig. 7. Coronal and transverse slice of the (a) reconstruction of the awake scan, (b) awake scan after motion correction using point source tracking, (c) motion-free scan using anesthesia and (d) template magnetic resonance image as an anatomical reference for the 3 rats.

In our experiments using the scanner default energy window (350 to 650 keV), for the sensitivity of our PET scanner (6.8 % at the center of the FOV), an activity between 148-222 kBq was enough to easily differentiate the point sources in approximate reconstructions of 15 ms acquisitions. The lower threshold for the point source activity was selected as low as possible while still being able to detect the point sources in the 32 ms reconstructions during the whole duration of the scan. The upper limit was selected to avoid too high activity as very high activity could lead to spill-over to brain regions. About 100 events came from each of the point sources in the 32 ms frames. Scanners with lower or higher sensitivity would require higher or lower point source activity respectively to identify the point sources.

The tracking frame rate is of importance to reduce the uncertainty between motion measurements. The motion corrected reconstructions using 66.7 Hz tracking frame rate showed better spatial resolution than those using 31.2 Hz. For instance, in the motion corrected microDerenzo phantom the FWHM of the 2.5 mm rods tracking at 31.2 Hz was 2.60 mm, which was reduced to 2.48 mm when tracking at 66.7 Hz. The benefits obtained by increasing the tracking frame rate are also dependent on the subject speed. For motion scans with irregular motion a high tracking frame rate is beneficial, however this comes at the cost of a higher computational processing.

The distance of the point sources to the subject activity is another important factor to differentiate the point sources from the background activity. If a point source is too close to a region with activity it might be difficult to recognize it in the short time frame reconstructions. In our experiments using [^{18}F]FDG, the closest distance of a point source to a region of activity was 3.5 mm (above the harderian gland). For tracers that accumulate in the skin or skull the point source tracking might require point sources with higher activity. In addition, the distance to the subject activity must be far enough to avoid spill-over artifacts in the reconstructions. In our experiments, the activity of the point sources was low enough and the distance to the brain large enough so we did not measure any spill-over artifacts stemming from these point sources.

The number of point sources used for tracking and their inter-point distances influence the accuracy of the motion data. Since the position in the pose is determined as the centroid of the point sources (average calculation), increasing the number of point sources improves the accuracy of the measurement. However the available space on the rat's head is limited. The distance between the point sources affects the accuracy of the pose orientation measurement. As the distance between the point sources increases, the uncertainty in the individual point source locations has a lower effect in the error of the orientation determination.

The slippage of the point sources due to the rat skin flexibility was handled by two strategies. First an average point set model considering all point sources position throughout the whole scan was considered. Secondly, frames were discarded either because the difference with the true inter-point distance was higher than a threshold (1.7 mm) or because the point-set registration to the reference failed (error > 1 mm).

For a typical 20 minutes rat brain PET scan, processing of the data for motion tracking at 31.2 Hz took about 125 minutes. The short time frame reconstructions and the image dilation operations are the most time consuming calculations. Although the reconstruction calculation was parallelized, the code was not optimized for parallel computing. Faster motion tracking times could be achieved by implementing optimal

parallel reconstruction algorithms [30] or by using GPU based image processing [31].

The tracking accuracy for translational motion along the axial axis with PST and OT was similar, with a mean error of 0.24 and 0.19 mm for PST and OT respectively. The error did not change for the different positions along the vertical axis. The tracking error, for both PST and OT, is well below the scanner spatial resolution.

Although OT has smaller translational tracking error than PST, the point source tracking outperformed our optical tracking implementation using a Micron Tracker camera in terms of spatial resolution of the motion corrected reconstructions of the resolution phantom. This might be due to differences in tracking performance of irregular motion and rotational motion. The error in the orientation measurement of the pose increases with smaller marker size for OT [22], an important requirement for rat head tracking to avoid discomfort on the rat. The orientation error is translated to increased positioning error for objects farther away from the marker center of rotation.

Filtering of the OT poses improved the motion corrected reconstructions in terms of spatial resolution. An improved spatial calibration between the optical tracker and the PET scanner could improve the OT motion corrected reconstructions. Adjusting the OT tracking frame rate could also improve the motion correction, however this was not considered as only one frame rate can be considered at a time given that the frame rate has to be set before the acquisition.

The point source tracking procedure proved to be feasible in *in vivo* practice and the experiments in rats were easily reproduced with good agreement (Bland-Altman limits of agreement) and correlation between regional uptake in the motion corrected image and the anesthesia reference scan. There was some resolution loss compared to the reference scan and this was assessed by the scale parameter of the motion corrected image. It should be noted that the scale parameter not only reflects loss of spatial resolution but also depends on noise level and on differences in [^{18}F]FDG uptake between the awake and anesthesia scan. Activity in the anesthesia scans is also reduced (-12% after 20 min) in comparison with the awake scans due to [^{18}F]FDG decay. The phantom experiment provides a better measure of resolution loss. Nonetheless the scale parameter is still a useful measure for in vivo comparison of motion tracking and motion correction methods provided similar imaging conditions are considered (e.g. scanner, noise level, uptake time).

The rats did not require training and showed no discomfort due to the presence of the point sources. The point sources were never detached from the head even when the rats were grooming. The cylindrical holder used to maintain the rat in the PET scanner also served to limit the motion of the rat inside the FOV during the whole scan. However with our current setup the rat head could move out of the FOV. If the rat head was outside the FOV for longer periods the holder was manually shifted so that the head was inside the FOV again. Our data suggest that for the third rat experiment the low tracking success rate was due to the rat spending more time outside the FOV compared to the other 2 scans.

The tracking success rate will also be affected by the speed of the rat head. Indeed the point sources in the IEM reconstructions will be more blurred at higher speeds which hampers the tracking. On average, the speed of the rat head was faster for the third rat experiment.

Simultaneous tracking of a rat with PST and OT was not considered as several factors would hamper a fair comparison. For example the checkerboard marker will cause additional skin slippage due to its weight. This in turn will negatively affect the accuracy of the PST method as also the point sources will move by this slippage. In addition, the rats tend to turn around inside the tube during the scan and, while with PST we could still track the motion, with OT those frames would be lost.

A drawback of the current implementation is the use of anesthesia to paste the point sources. Training the rats to paste the point sources while awake is a possible solution. Another solution could make use of point sources using PET isotopes with longer half-life's, such as ^{64}Cu or ^{89}Zr. The point sources made with these radionuclides could be, for instance, pasted the day before the experiment. Alternatively ^{18}F point sources with increased activity could be pasted several hours before the start of the experiment.

In our *in vivo* experiments [^{18}F]FDG scans were acquired. This was primarily to illustrate the feasibility of the method and to have access to a reference scan. Indeed, for this irreversible tracer, uptake reaches a plateau after a certain uptake period, so that the tracer is effectively trapped inside the cells. Therefore the tracer distribution during the scan under anesthesia was expected to be very similar to the tracer distribution during the awake scan. The benefit of awake animal scanning for this kind of tracers that can be imaged after an awake uptake period is limited. However, for many other tracers (e.g. reversible tracers such as [^{11}C]-raclopride) dynamic scanning is required and awake animal scanning is expected to be very relevant for these tracers.

Finally, future work involves exploring the implementation of the technique in rat brain awake scans using different radiotracers, e.g. ^{11}C labeled radiotracers, and test the procedure in different PET scanners, including human scanners for motion correction in human brain scans. Factors such as the scanner spatial resolution, sensitivity, FOV size and bore size must be investigated to assess the feasibility. In human studies special consideration must be taken so as to limit the additional dose imparted by the point sources.

V. Conclusions

The feasibility to perform fast rigid body motion tracking during PET scanning using radioactive point sources was demonstrated in phantom and awake rat experiments. The point source tracking outperformed our optical tracking implementation in terms of the image resolution of the motion corrected image of the resolution phantom. The PET scans of the awake rats were successfully corrected for motion using the point source tracking motion data. The point sources were well tolerated by the rat and allowed free motion of the head.

The tracking is performed using the PET scanner itself and the technique is suitable for small-bore PET scanners where optical tracking can be challenging.

ACKNOWLEDGEMENTS

Authors would like to thank Philippe Joye and Caroline Berghmans for the assistance on *in vivo* experiments. This work was supported by the UA BOF-GOA 2013 (FFB6244) grant and by the FWO grants GOA8517N and 1520217N.

APPENDIX I

This appendix presents the pseudocode for the point source tracking algorithm.

Define number of point sources P and inter-point distances m_l
Divide list-mode data in short time frames
For each time frame
  Reconstruct LORs in time frame (either IB or IEM)
  If previous frame tracking was correct
    Reduce image volume to a neighborhood around previous point source positions
  Else
    Use complete image
  End

  Calculate image dilation and select local maxima (N)
  If previous frame tracking was correct
    For each point source P
      Calculate distance from previous location to all local maxima N
      Select closest point within 3 mm
    End
    If a point was found within 3 mm for each point source
      Select point sources location
      Further refine point source locations
      Continue with next frame
    End
  End

  For each local maxima N
    Calculate score S_n based on volume and compactness
  End
  With 10 highest scores S_n calculate inter-point distance matrix
  discard groups with at least one inter-point distance D_l^g greater than threshold

  For every group g
    Calculate error E_g
  End
  If at least one group E_g is whitin threshold
    Select group g with smallest E_g
    Further refine point source locations
    Continue with next frame
  Else
    Tracking fails
    Continue with next frame
  End
End
Calculate point source array poses

Fig. 8. Pseudocode of the point source tracking algorithm

REFERENCES

[1] A. K. Alstrup, A. M. Landau, J. E. Holden *et al.*, "Effects of anesthesia and species on the uptake or binding of radioligands in vivo in the Gottingen minipig," *BioMed research international*, vol. 2013, pp. 808713, 2013.

[2] A. Matsumura, S. Mizokawa, M. Tanaka *et al.*, "Assessment of microPET performance in analyzing the rat brain under different types of anesthesia: comparison between quantitative data obtained with microPET and ex vivo autoradiography," *NeuroImage*, vol. 20, no. 4, pp. 2040-50, Dec, 2003.

[3] B. J. Fueger, J. Czernin, I. Hildebrandt *et al.*, "Impact of animal handling on the results of 18F-FDG PET studies in mice," *Journal of nuclear medicine : official publication, Society of Nuclear Medicine*, vol. 47, no. 6, pp. 999-1006, Jun, 2006.

[4] S. Momosaki, K. Hatano, Y. Kawasumi *et al.*, "Rat-PET study without anesthesia: anesthetics modify the dopamine D1 receptor binding in rat brain," *Synapse*, vol. 54, no. 4, pp. 207-13, Dec 15, 2004.

[5] K. K. Sung, D. P. Jang, S. Lee *et al.*, "Neural responses in rat brain during acute immobilization stress: a [F-18]FDG micro PET imaging study," *NeuroImage*, vol. 44, no. 3, pp. 1074-80, Feb 1, 2009.

[6] V. D. Patel, D. E. Lee, D. L. Alexoff *et al.*, "Imaging dopamine release with Positron Emission Tomography (PET) and (11)C-raclopride in freely moving animals," *NeuroImage*, vol. 41, no. 3, pp. 1051-66, Jul 1, 2008.

[7] M. Akhtar, A. Kyme, V. Zhou *et al.*, "An investigation of the challenges in reconstructing PET images of a freely moving animal," *Australas Phys Eng Sci Med*, 4, 2013, pp. 405-15.

[8] V. Zhou, J. Eisenhuth, A. Kyme *et al.*, "A Motion Adaptive Animal Chamber for PET Imaging of Freely Moving Animals," *Ieee T Nucl Sci*, vol. 60, no. 5, pp. 3423-3431, Oct, 2013.

[9] C. Woody, P. Vaska, D. Schlyer *et al.*, "Initial studies using the RatCAP conscious animal PET tomograph," *Nucl Instrum Meth A*, vol. 571, no. 1-2, pp. 14-17, Feb 1, 2007.

[10] D. Schulz, S. Southekal, S. S. Junnarkar *et al.*, "Simultaneous assessment of rodent behavior and neurochemistry using a miniature positron emission tomograph," *Nature methods*, vol. 8, no. 4, pp. 347-52, Apr, 2011.

[11] A. Z. Kyme, V. W. Zhou, S. R. Meikle *et al.*, "Real-time 3D motion tracking for small animal brain PET," *Physics in medicine and biology*, vol. 53, no. 10, pp. 2651-66, May 21, 2008.

[12] A. Z. Kyme, V. W. Zhou, S. R. Meikle *et al.*, "Optimised motion tracking for positron emission tomography studies of brain function in awake rats," *PloS one*, vol. 6, no. 7, pp. e21727, 2011.

[13] A. Kyme, S. Se, S. Meikle *et al.*, "Markerless motion tracking of awake animals in positron emission tomography," *IEEE transactions on medical imaging*, vol. 33, no. 11, pp. 2180-90, Nov, 2014.

[14] A. Miranda, J. Verhaeghe, J. Parthoens, S. Stroobants and S. Staelens, "Motion uncertainty deblurring in motion corrected reconstruction for PET brain imaging of awake rats," *IEEE Nuclear Science Symposium and Medical Imaging Conference (NSS/MIC)*, Seattle, WA, 2014

[15] E. P. Visser, J. A. Disselhorst, M. Brom *et al.*, "Spatial resolution and sensitivity of the Inveon small-animal PET scanner," *Journal of nuclear medicine : official publication, Society of Nuclear Medicine*, vol. 50, no. 1, pp. 139-47, Jan, 2009.

[16] A. Rahmim, M. Lenox, A. J. Reader *et al.*, "Statistical list-mode image reconstruction for the high resolution research tomograph," *Physics in medicine and biology*, vol. 49, no. 18, pp. 4239-58, Sep 21, 2004.

[17] F. Jacobs, E. Sundermann, M. Christiaens *et al.*, "A fast algorithm to calculate the exact radiological path through a pixel or voxel space," *Journal Of Computing and Information Technology*, vol. 6, no. 1, pp. 89-54, 1998.

[18] R. C. Gonzalez, and R. E. Woods, *Digital image processing*, 2nd ed., Upper Saddle River, N.J.: Prentice Hall, 2002.

[19] C. A. Martinez-Ortiz, "2D and 3D shape descriptors," Thesis (Ph.D.) - Exeter University, College of Engineering, Mathematics and Physical Sciences., Exeter,, 2010.

[20] D. J. Parker, C. J. Broadbent, P. Fowles *et al.*, "Positron Emission Particle Tracking - a Technique for Studying Flow within Engineering Equipment," *Nucl Instrum Meth A*, vol. 326, no. 3, pp. 592-607, Mar 10, 1993.

[21] P. J. Besl, and N. D. Mckay, "A Method for Registration of 3-D Shapes," *Ieee T Pattern Anal*, vol. 14, no. 2, pp. 239-256, Feb, 1992.

[22] A. Kyme, J. Maclaren, S. Meikle, C. Baldock, R. Fulton, "The Effect of Time Domain Pose Filtering on Accuracy of Small Marker Based Motion Correction in Awake Animal PET," *2011 Ieee Nuclear Science Symposium and Medical Imaging Conference (Nss/Mic)*, pp. 2290-4, 2011.

[23] M. G. Spangler-Bickell, L. Zhou, A. Z. Kyme, B. De Laat, R. R. Fulton, J. Nuyts, "Optimising rigid motion compensation for small animal brain PET imaging," *Physics in medicine and biology*, vol. 61, no. 19, pp. 7074-91, Oct, 2016

[24] W. K. Schiffer, M. M. Mirrione, A. Biegon *et al.*, "Serial microPET measures of the metabolic reaction to a microdialysis probe implant,"

Journal of neuroscience methods, vol. 155, no. 2, pp. 272-84, Sep 15, 2006.

[25] D. Giavarina, "Understanding Bland Altman analysis," *Biochemia medica*, vol. 25, pp. 141-51, 2015

[26] A. J. Reader, "List-mode EM algorithms for limited precision high-resolution PET image reconstruction," *Int J Imag Syst Tech*, vol. 14, no. 3, pp. 139-145, 2004.

[27] A. J. Reader, P. J. Julyan, H. Williams *et al.*, "EM algorithm system modeling by image-space techniques for PET reconstruction," *Ieee T Nucl Sci*, vol. 50, no. 5, pp. 1392-1397, Oct, 2003.

[28] A. Rahmim, P. Bloomfield, S. Houle *et al.*, "Motion compensation in histogram-mode and list-mode EM reconstructions: Beyond the event-driven approach," *Ieee T Nucl Sci*, vol. 51, no. 5, pp. 2588-2596, Oct, 2004.

[29] J. Babaud, A. P. Witkin, M. Baudin and R. O. Duda "Uniqueness of the gaussian kernel for scale-space filtering," *IEEE Trans Pattern Anal Mach Intell*, vol. 8, pp. 26-33, 1986.

[30] H. Gao, "Fast parallel algorithms for the x-ray transform and its adjoint," *Medical physics*, vol. 39, no. 11, pp. 7110-20, Nov, 2012.

[31] X. Jia, P. Ziegenhein, and S. B. Jiang, "GPU-based high-performance computing for radiation therapy," *Physics in medicine and biology*, vol. 59, no. 4, pp. R151-82, Feb 21, 2014.